ACS OMEGA

http://pubs.acs.org/journal/acsodf

Article

Development of Boron-Doped Mesoporous Carbon Materials for Use in CO_2 Capture and Electrochemical Generation of H_2O_2

Jinhao Li, Chao Shi, Agula Bao,* and Jingchun Jia

Cite This: *ACS Omega* 2021, 6, 8438−8446

Read Online

ACCESS | Metrics & More | Article Recommendations

ABSTRACT: Mesoporous carbon materials have been increasingly studied due to their large specific surface area and good chemical stability. Optimizing their functionality through a doping modification can broaden their application in many fields. Herein, a series of B-doped mesoporous carbon materials are prepared by a convenient hydrothermal synthesis using F127 as the template and boric acid as the boron source. The whole material preparation process meets the requirements of green chemistry. Notably, the prepared carbon materials not only exhibit good electrocatalytic oxygen reduction to hydrogen peroxide in alkaline media but also have an excellent CO_2 adsorption capacity (up to 121.34 mg/g) at 303 K and atmospheric pressure. These results show that the prepared samples can be utilized as multifunctional materials for handling a variety of environmental issues.

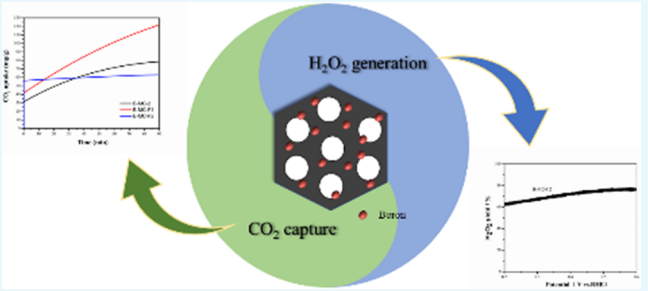

1. INTRODUCTION

As human society continues to industrialize and urbanize, environmental issues have become one of the most severe challenges facing mankind in the 21st century.[1] Therefore, we need to make large breakthroughs for decreasing or removing environmental pollution. Many researchers rated water pollution and global warming as top public concerns.[2,3] In terms of sewage treatments, hydrogen peroxide (H_2O_2) is an environmentally friendly strong oxidant that can remove harmful microorganisms and some persistent organic pollutants in water.[4] More importantly, the decomposition products of H_2O_2 are water and oxygen; thus, the use of H_2O_2 does not produce environmentally hazardous byproducts. Compared with the direct synthesis of H_2O_2 from H_2 and O_2 and other preparation methods that clearly have safety hazards, electrocatalytic oxygen reduction provides a green and efficient way to generate H_2O_2 through a two-electron pathway.[5−8] In addition to water pollution, the problem of global warming caused by the release of CO_2 by fossil fuels in the production of chemical products has also had a very large negative impact on our lives.[9−11] Therefore, the effective capture of CO_2 is imperative and imminent. From the perspective of sustainable development, it is desirable to find a new material that can deal with a variety of environmental problems.

With the introduction and development of nonmetallic catalysis, carbon materials have become important functional materials developed recently; the surface chemical properties of carbon materials can be flexibly controlled, and their performance can vary over a wide range, exhibiting semiconducting characteristics as well.[12−14] Based on the above advantages, activated carbon,[15] activated carbon fiber,[16] graphene,[17] and mesoporous carbon[18] have been increasingly studied by researchers. Among them, mesoporous carbon (pore sizes of 2−50 nm) is a new type of inorganic nonmetallic carbon silica.[19] Mesoporous carbon not only has the characteristics of easy surface modifications, a good heat conduction, and good electron transport performance but also has an optimized pore structure, surface multiplicity, and stable properties compared with other carbon materials.[20,21] Many studies have suggested that the functional properties of mesoporous carbon are closely related to its surface chemical properties (quantity of defects and surface functional groups).[22,23] Accordingly, modifications with heteroatoms, such as nitrogen,[24] oxygen,[25] phosphorus,[26] and boron,[27] can break the inherent delocalized π-structure of the carbon material skeleton and optimize its surface characteristics.[28−30] Among them, nitrogen, as the most common dopant, has established applications in many fields. Wei et al.[31] used dicyandiamide (DCDA) as a nitrogen source and resol as a carbon source to prepare an N-doped mesoporous carbon material and applied it to a CO_2 adsorption experiment. The results showed that when using a 2.5:1 mass ratio of DCDA to

Received: January 12, 2021
Accepted: March 10, 2021
Published: March 22, 2021

https://doi.org/10.1021/acsomega.1c00197
ACS Omega 2021, 6, 8438−8446

resol at 298 K and 100 kPa, the sample prepared by KOH activation had a high CO_2 adsorption capacity (up to 3.2 mmol/g). Park et al.[32] used silica KIT-6 as a hard template, furfuryl alcohol as a carbon source, and (1-methyl-1*H*-pyrrol-2-yl) methanol as a nitrogen source to successfully synthesize a series of N-doped mesoporous carbon materials. The synthesized carbons exhibited good catalytic activity for preparing H_2O_2 by electrochemical oxygen reduction. Compared with N-doped carbon materials, there are few reports of B-doped carbon applied in the electrocatalytic production of hydrogen peroxide or in CO_2 capture. Boron has only one electron less than carbon and their sizes are similar, which leads to the lattice distortion of graphite after relatively small boron doping.[33,34] Therefore, B can also be an ideal dopant in carbon materials.

In previous studies, most of the B-doped mesoporous carbon materials were prepared by the hard template method. Bo et al.[35] used sucrose and 4-hydroxyphenylboronic acid as the raw materials, and SBA-15 was used as a hard template; the mass ratio of 4-hydroxyphenylboronic acid/sucrose was adjusted to prepare B-doped mesoporous carbon materials. Compared with the material without B, the carbon material doped with B had an ordered mesoporous structure and a high boron content. This feature allowed the material to have an onset potential of −0.16 V during the oxygen reduction reaction (ORR) test. Although the hard template method can control the synthesis of mesoporous carbon by changing the external structure of the template, there are still some shortcomings in this method, such as the residual template material and tedious/time-consuming preparation process. Until now, there is no effective method to make up for these deficiencies. Furthermore, in many respects, the hard template method is still difficult to utilize in the mass synthesis of mesoporous carbon materials.[36] In comparison, the soft template method is more feasible and scalable because this method does not require prefabricated template materials and is easier to operate.

In this paper, F127 and boric acid are used as the soft template and boron source, respectively, and a series of B-doped mesoporous carbon materials are prepared by changing the molar ratio of boron to carbon and the amount of added F127. All prepared samples have a high specific surface area, uniform pore diameter, and regular mesoporous structure. Experimental results show that the carbon materials modified by B have good performance in both electrocatalytic oxygen reduction to produce hydrogen peroxide and CO_2 capture. This result is mainly because the introduction of B has a positive effect in improving the electron-deficient active center of the samples. The addition of B causes the material to exhibit P-type semiconductor properties, which can improve the hole transport properties of carbon and increase the graphitization and oxidation resistance of the materials.

2. RESULTS AND DISCUSSION

2.1. Structural Characterization. To prepare B-doped mesoporous carbon materials with a controllable structure and morphology, samples with different B/C molar ratios and template doses were characterized by transmission electron microscopy (TEM). Here, B-MC-2, B-MC-3, B-MC-F1, and B-MC-F2 were used as examples. Figure 1a and b shows the TEM images of B-MC-2 and B-MC-3, respectively. The figure shows that B-MC-2 has a hexagonal mesoporous structure, which is conducive to mass transfer in the catalytic process.[37]

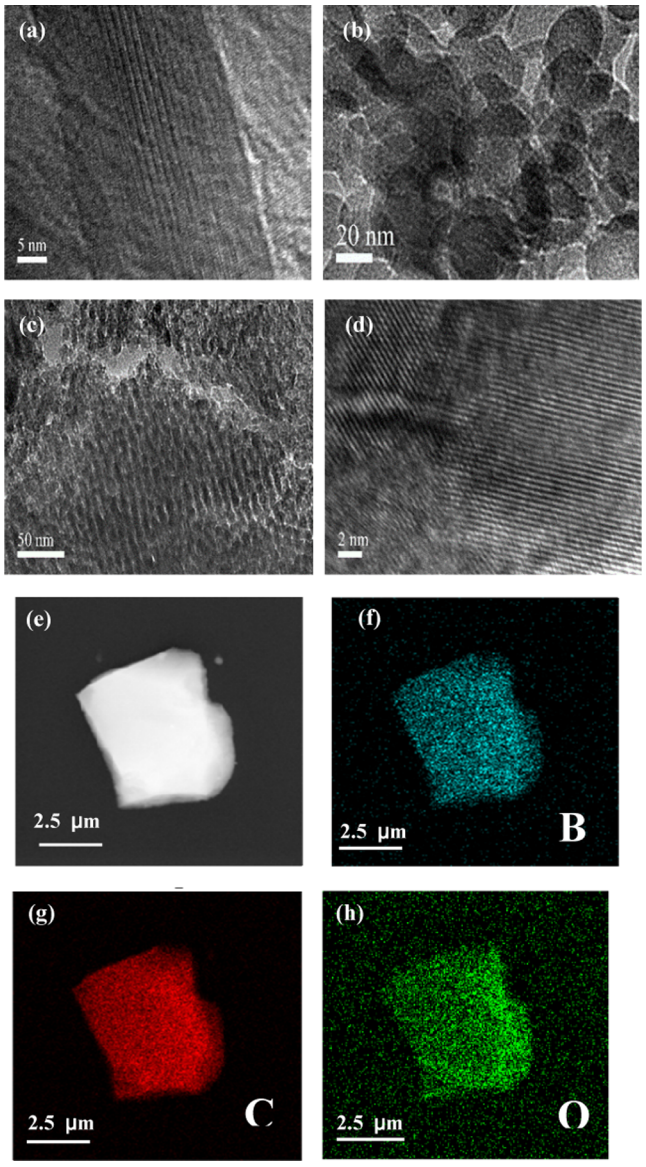

Figure 1. TEM images of (a) B-MC-2, (b) B-MC-3, (c) B-MC-F1, and (d) B-MC-F2. (e−h) EDS elemental mappings of B-MC-F1.

Remarkably, B-MC-3 prepared with more boron shows an irregular mesoporous structure in the TEM images. This result is due to the addition of a large amount of B in the framework, which distorts the carbon lattice and causes an irregular pore structure. Figure 1c and d shows the TEM images of B-MC-F1 and B-MC-F2, respectively. Both the samples have clearly arranged mesopores, but with the change in the quantitative amount of the F127 template, there are clear differences in the degree of ordering in the structure of the sample. It follows that the appropriate amount of B doping and F127 has a certain effect on the pore structure of the material. The energy-dispersive spectroscopy (EDS) elemental mapping method was used to further study the distribution of B in B-MC-F1. As shown in Figure 1e−h, B is uniformly distributed in B-MC-F1, confirming the success of B doping into the carbon skeleton.

X-ray diffraction (XRD) is an important method for determining the crystal structure. As revealed in Figure 2a, all samples have two obvious peaks at 23 and 43°, which can be indexed to the (0 0 2) and (1 0 0) lattice planes of graphitic carbons, respectively. In addition, the changing contents of

https://doi.org/10.1021/acsomega.1c00197
ACS Omega 2021, 6, 8438−8446

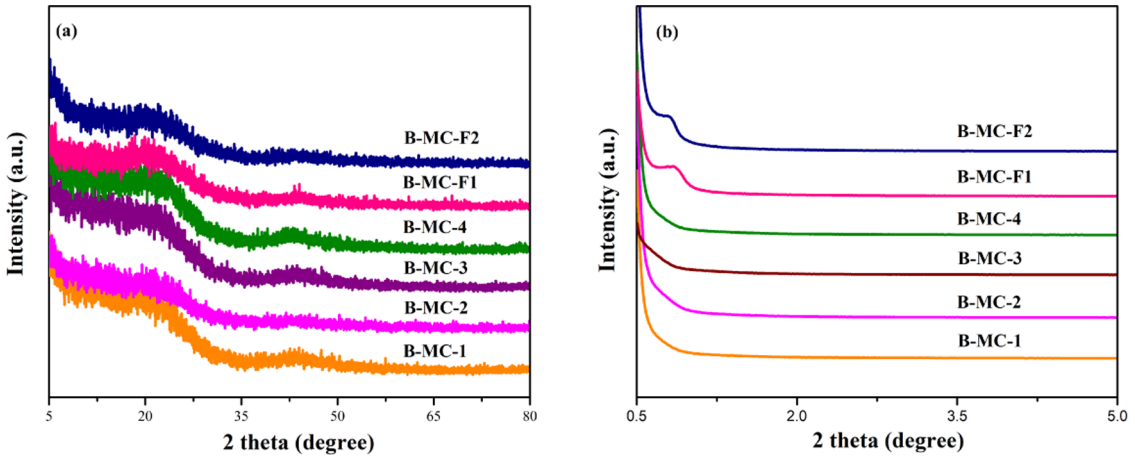

Figure 2. (a) Wide-angle XRD pattern of B-MC-*X* and B-MC-F*X*. (b) Small-angle XRD pattern of B-MC-*X* and B-MC-F*X*.

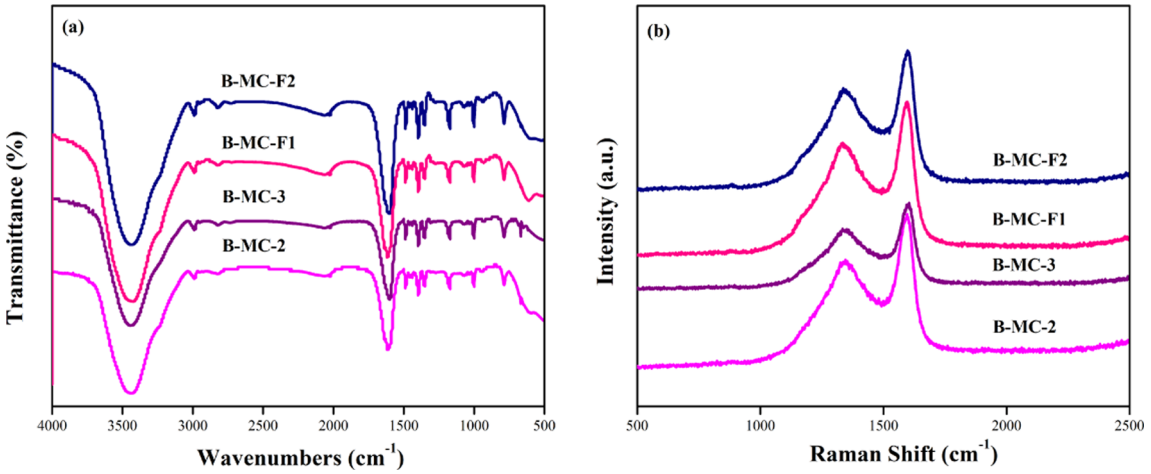

Figure 3. (a) FTIR spectra of B-MC-2, B-MC-3, B-MC-F1, and B-MC-F2. (b) Raman spectra of B-MC-2, B-MC-3, B-MC-F1, and B-MC-F2.

boron and F127 affect the intensity of the diffraction peak. When the B/C molar ratio reaches 0.075, the intensity of the diffraction peak reaches its maximum value. Subsequently, when the B/C molar ratio continues to increase, the diffraction peak intensity gradually decreases. As the amount of F127 increases, the intensities of the diffraction peaks also increase. Figure 2b shows the small-angle XRD pattern of all samples. Some carbons exhibit a single diffraction peak of approximately 0.7° (samples B-MC-F1 and B-MC-F2). This peak originates from a periodic pore-to-pore correlation. This indicates that ordering is observed for B-MC-F1 and B-MC-F2; other materials are mostly disordered.

Figure 3a shows the Fourier transform infrared spectroscopy (FTIR) spectra of B-MC-2, B-MC-3, B-MC-F1, and B-MC-F2. This figure shows that there are strong absorption peaks at 3438, 2990, and 1170 cm^{-1}, which correspond to the stretching vibration peaks of O−H, C−H, and C−O.[38] The characteristic peaks at 1490 and 1610 cm^{-1} are due to the skeleton vibration absorptions of the C═C in the benzene ring. Furthermore, the absorption peak at 1360 cm^{-1} is the stretching vibration peak of BO_3, and the characteristic peak at 1000 cm^{-1} is the rocking vibration peak of B−C.[39,40] As shown by Raman spectroscopy (Figure 3b), there are two main characteristic bands in the spectrum, the D band and the G band, which are at approximately 1350 and 1593 cm^{-1}, respectively. When the structural characteristics of carbon nanomaterials are analyzed by Raman spectroscopy, we usually use the intensity ratio of the D peak to the G peak (I_D/I_G) to evaluate the disorder and defect content of the material structure.[11] This calculation shows that the I_D/I_G values of B-MC-2, B-MC-3, B-MC-F1, and B-MC-F2 are 0.84, 0.86, 0.76, and 0.75, respectively. It is worth noting that the I_D/I_G value of B-MC-3 is higher than that of B-MC-2, which proves that the addition of B causes the material to exhibit more defect sites. The I_D/I_G value decreases significantly from B-MC-2 to B-MC-F1 and B-MC-F2, revealing that the graphitization degree of B-MC-F2 is enhanced due to the change in the amount of F127.

To further study the influence of the boron doping amount and the state in the carbon material, X-ray photoelectron spectroscopy (XPS) measurements were carried out. As seen in the full spectra (Figure 4a), the peak at 192.7 eV is a B 1s signal, and the peaks at 285.0 and 533.0 eV are the signals of C 1s and O 1s, respectively. The B 1s spectrum of B-MC-F1 (Figure 4b) is fitted into two peaks at approximately 195.0 and 191.0 eV, which can be attributed to the characteristic peaks of BC_3 and BCO_2/BC_2O, respectively. BCO_2/BC_2O are the main B-doped phases in the carbon layer. This is because boron is more likely to combine with oxygen and carbon atoms. According to the report, different types of boron bonds in B-doped carbon materials have different contributions to catalysis and adsorption. In regard to the C 1s spectrum (Figure 4c), C═C (284.8 eV), C−O (286.0 eV), and O═C−O (289.0

https://doi.org/10.1021/acsomega.1c00197
ACS Omega 2021, 6, 8438−8446

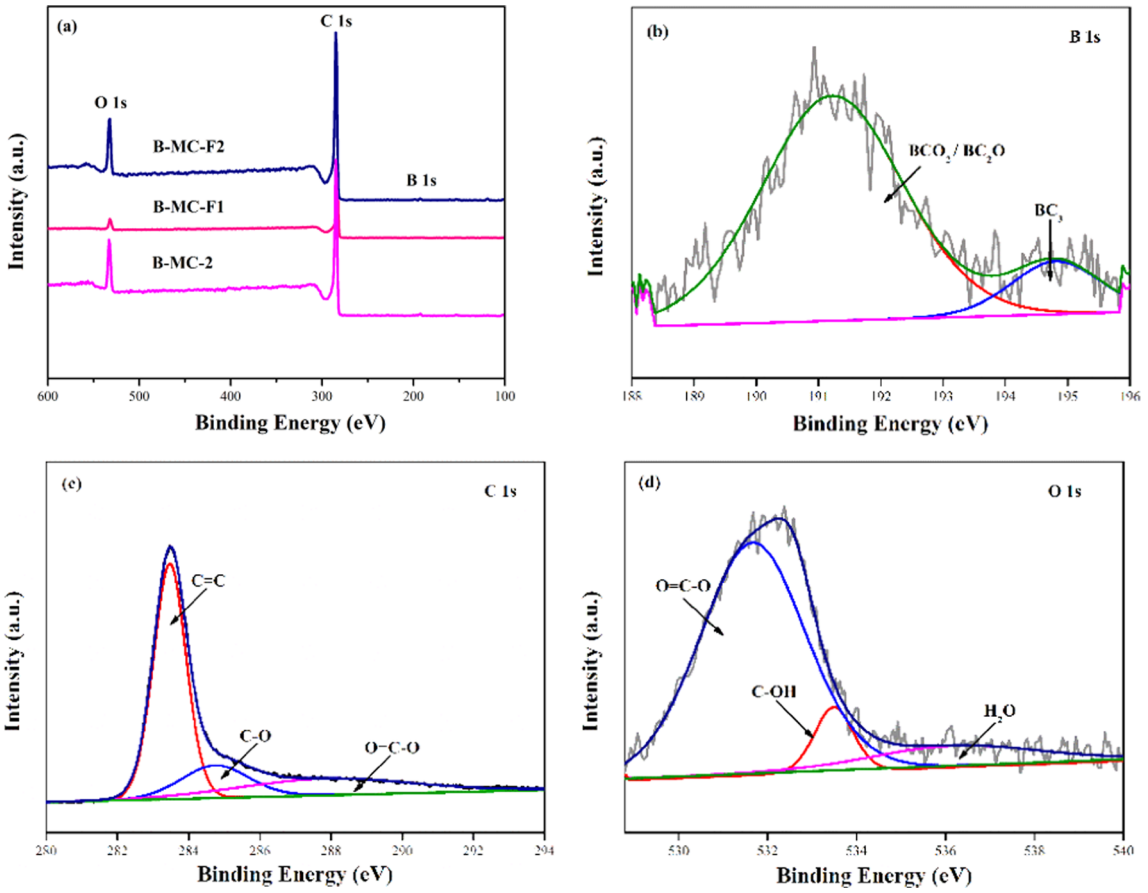

Figure 4. (a) XPS survey spectra of B-MC-2, B-MC-F1, and B-MC-F2. (b–d) High-resolution B 1s, C 1s, and O 1s XPS spectra of B-MC-F1.

eV) are observed. Additionally, O═C−O (532.5 eV), C−OH (533.8 eV), and H_2O (534.7 eV) are observed in the O 1s fine spectrum (Figure 4d).[41] The content distribution of each element is shown in Table 1. This table shows that with the increase in the B/C molar ratio, the content of boron and oxygen species in the materials also increases. This result may be because BCO_2/BC_2O in the synthetic material are the main doping phases of B in the carbon layer. With the increase in the F127 content, the amount of boron species increases but the content of oxygen species decreases. It is rather remarkable that the long-range two-dimensional (2D) ordering of defective graphene layers forming the most porous carbons can be affected by the doping with B. At the same time, introducing more surface groups with O can contribute to cross-linking between stacked graphene domains. This result

Table 1. Boron, Carbon, and Oxygen Species on the Surface of the Prepared Materials

sample	B 1s (atom %)	C 1s (atom %)	O 1s (atom %)
B-MC-2	0.4	89.01	10.6
B-MC-F1	1.27	90.54	8.19
B-MC-F2	0.59	86.93	12.47

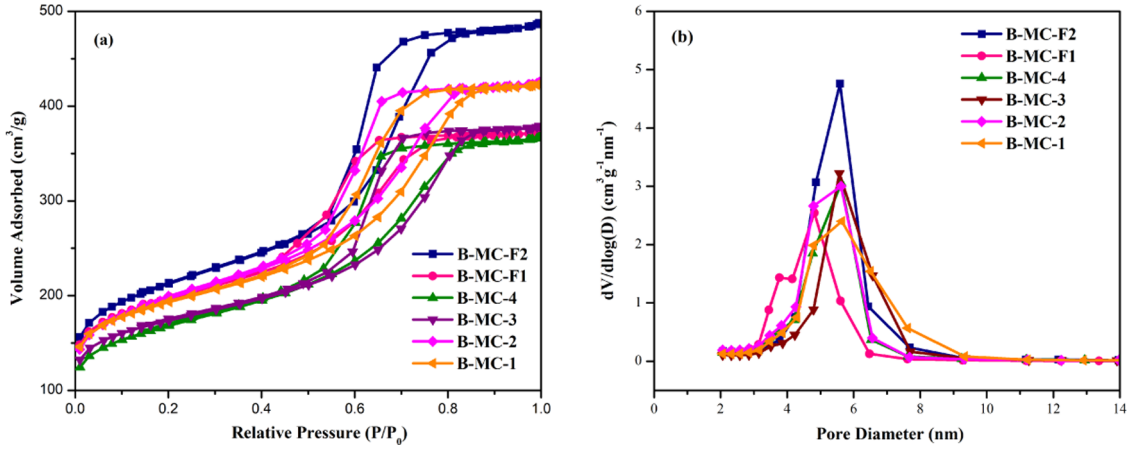

Figure 5. (a) N_2 adsorption−desorption isotherms of B-MC-*X* and B-MC-F*X*. (b) Pore size distributions of B-MC-*X* and B-MC-F*X*.

https://doi.org/10.1021/acsomega.1c00197
ACS Omega 2021, 6, 8438−8446

may lead to B-MC-F2 with better catalytic activity in the ORR process.

Figure 5a depicts the N_2 adsorption−desorption isotherms of B-MC-*X* and B-MC-F*X*. All samples have type IV isotherms in the relative pressure range of 0.5−0.8; additionally, a typical H2 hysteresis loop appears, which shows that these materials have mesoporous structures.[19] As demonstrated in Figure 5b, the pore size of all carbon materials is uniform, and the average pore size distribution has a smaller range, which proves that changing the amount of boric acid and F127 does not significantly affect the pore size of the material. Table 2 shows the corresponding textual properties of the samples. For the most part, the specific surface area of the carbon material is approximately 500−800 m^2/g and the average pore size is concentrated at approximately 4 nm. Furthermore, compared with the series of B-MC-*X* materials, the specific surface areas of the B-MC-F*X* series of materials increase, which may be due to the influence of the template dose on the structure of the materials.

Table 2. Physicochemical Properties of the Mesoporous Carbon Materials

sample	specific surface area (m^2/g)	pore volume (cm^2/g)	pore size (nm)
B-MC-1	667	0.65	3.90
B-MC-2	685	0.63	3.81
B-MC-3	600	0.58	3.88
B-MC-4	584	0.56	3.86
B-MC-F1	681	0.57	3.37
B-MC-F2	738	0.74	4.05

2.2. Material Applications. *2.2.1. Electrocatalytic 2e⁻ ORR for H_2O_2 Production.* To explore the electrocatalytic 2e⁻ ORR activity of the produced materials, CV measurements were obtained for the catalyst in 0.1 M KOH and with a scanning rate of 50 mV/s. In Figure 6a, we can clearly observe that B-MC-2 and B-MC-F2 show no characteristic electrocatalytic oxygen reduction peak in the Ar-saturated solution but do show a peak in the O_2-saturated electrolyte. The area under the B-MC-F2 curve is larger than that under the B-MC-2 curve, indicating that it has a higher electroactive surface area and superior ORR activity.

Previous studies have shown that the electrocatalytic activity of catalysts is mainly related to two parameters, namely, the specific surface area and pore structure. First, the specific surface area has some connection with the exposure of active centers. Second, the pore structure directly affects the mass transfer during electrocatalysis, and H_2O_2 produced by electrocatalysis can be released in a short contact time under the action of a mesoporous catalyst. It is worth noting that the highly ordered mesoporous structure has a higher selectivity toward H_2O_2.[32,32] In view of the influence of the boric acid and template content on the structure of the catalyst, the ORR activity of the catalyst with different boron-to-carbon molar

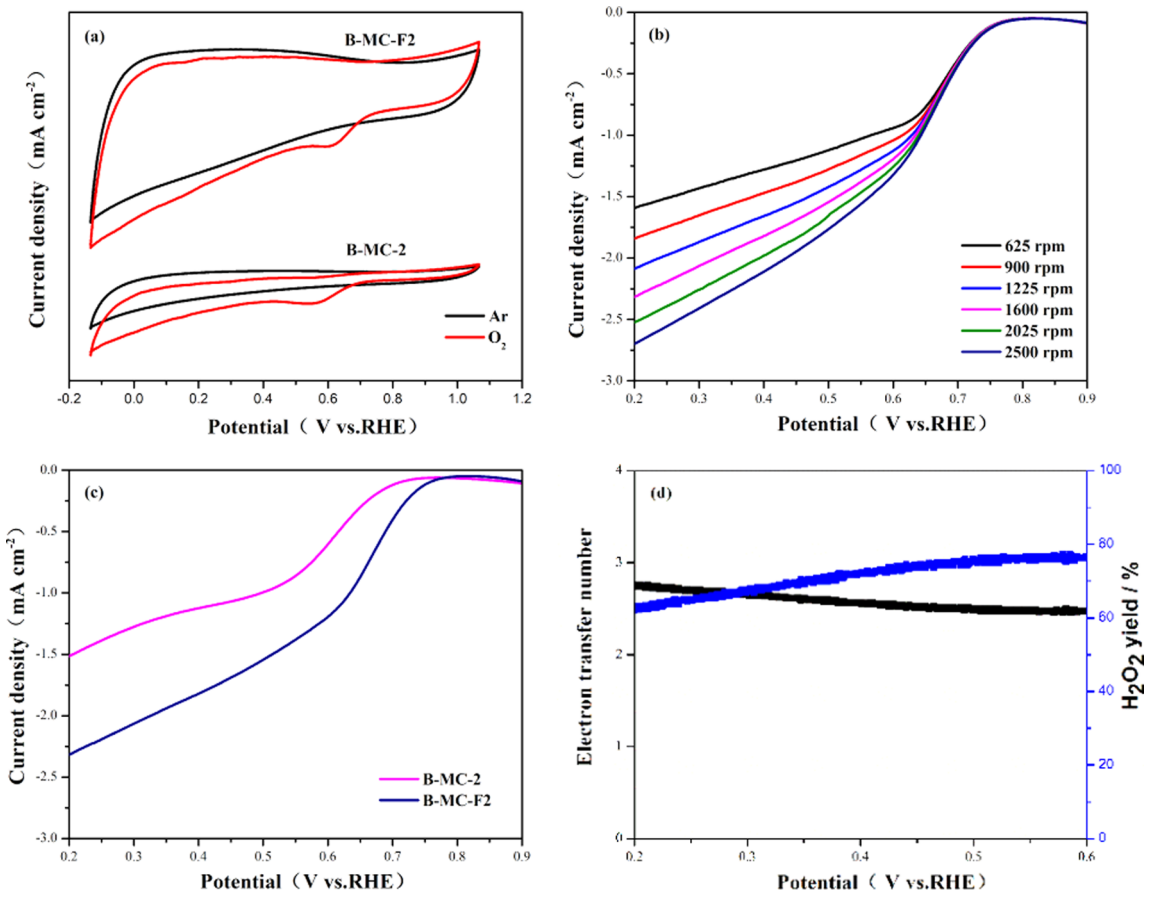

Figure 6. (a) Cyclic voltammetry curves of B-MC-2 and B-MC-F2 under O_2- and N_2-saturated conditions (scan rate: 50 mV/s). (b) Linear sweep voltammetry (LSV) curves of the ORR on B-MC-F2 at different rotation speeds. (c) LSV curves of B-MC-2 and B-MC-F2 at 1600 rpm. (d) Number of transferred electrons (*n*) when using B-MC-F2 and its H_2O_2 yield.

https://doi.org/10.1021/acsomega.1c00197
ACS Omega 2021, 6, 8438−8446

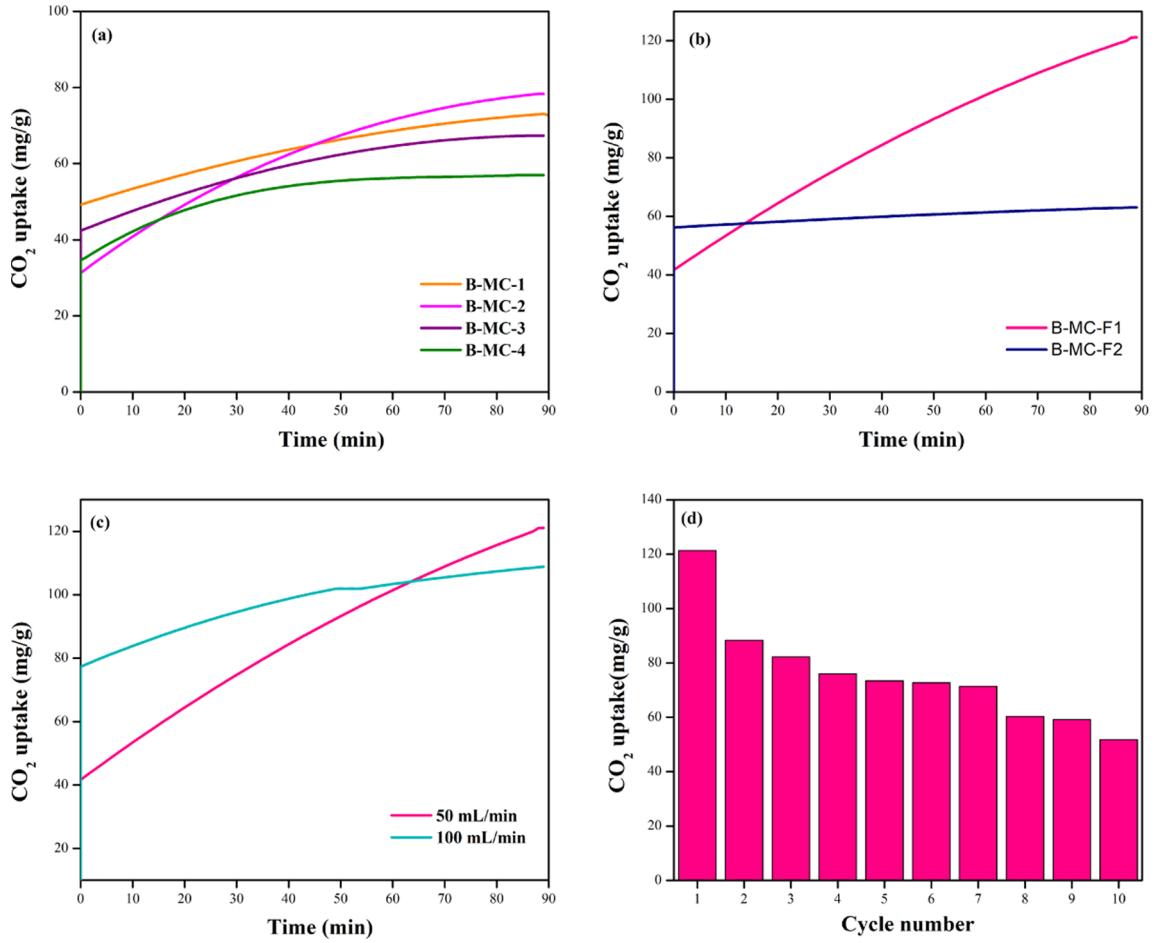

Figure 7. (a, b) CO_2 adsorption curves of B-MC-*X* and B-MC-F*X*. (c) Adsorption curves of B-MC-F1 at different CO_2 flow rates. (d) Study on the cycling stability of B-MC-F1.

ratios and F127 amounts was studied. Compared with the B-MC-*X* series, B-MC-F2 has a higher specific surface area (up to 738 m^2/g) and more abundant mesoporous structures; thus, it has more active centers for the ORR. Furthermore, the large total pore volume (0.74 cm^3/g) and pore size (4.05 nm) of B-MC-F2 contribute to its fast ORR kinetics. Although B-MC-F1 has a high boron content, its specific surface area and pore volume are lower than those of B-MC-F2, which decreases the activity of B-MC-F1.

Figure 6b,c shows the LSV curves of B-MC-F2 from 625 to 2500 rpm and the LSV curves of B-MC-2 and B-MC-F2 at 1600 rpm in 0.1 M KOH. Compared with B-MC-2, B-MC-F2 shows higher activity, with a corrected E_{onset} of 0.82 V. The poor catalytic activity of B-MC-2 may be due to the excessive addition of F127, which will change the pore structure, thereby affecting the catalytic activity. According to reports, the activity of the $2e^-$ ORR is mainly determined by the content of O in the material.[42] Therefore, an rotating ring disk electrode (RRDE) was used to observe the selectivity of the ORR on B-MC-F2 with the highest O content (up to 12.47 atom %) (Figure 6d). B-MC-F2 exhibits a significant $2e^-$ migration process ($n < 2.7$) and a relatively high H_2O_2 yield (up to 77%) in a wide voltage range, indicating that boron-doped mesoporous carbon materials can be used as excellent catalysts for the generation of H_2O_2.

2.2.2. CO_2 Capture Property. Considering that B-MC-*X* and B-MC-F*X* have good mesoporosity and a rich B content, they can be used as ideal CO_2 capture materials. From the adsorption isotherm (Figure 7a), it can be clearly seen that the CO_2 adsorption capacity of B-MC-*X* follows the order B-MC-2 > B-MC-1 > B-MC-3 > B-MC-4. When the B/C molar ratio is 0.05, the CO_2 uptake capacity of the material is the best, which may be due to the influence of the degrees of defects and the specific surface area of the samples on the CO_2 adsorption performance. As the template dose changes, the changes in the adsorption capacity of the materials are exhibited in Figure 7b. When the amount of template is 0.5 mmol, the material has excellent adsorption performance (121.34 mg/g), which is not only far higher than that of the B-MC-*X* series samples but also comparable to that of other B-doped mesoporous carbon materials.[43−47] Such results should be ascribed to the increase in the specific surface area and the boron content caused by the change in the template dose, which provides more active sites for the material.

Further tests were carried out with B-MC-F1, which has the best CO_2 adsorption performance, and the influence of the CO_2 gas flow rate on the adsorption capacity of the sample was studied. Figure 7c is a comparative graph of the CO_2 adsorption capacity of B-MC-F1 at CO_2 flow rates of 50 and 100 mL/min. When the CO_2 flow rate is 50 mL/min, the adsorption efficiency of this material is clearly higher. Referring to the calculations, when the CO_2 flow rate is increased to 100 mL/min, the adsorption capacity of this material decreases to 108.83 mg/g. Therefore, the appropriate adsorption rate will

https://doi.org/10.1021/acsomega.1c00197
ACS Omega 2021, 6, 8438−8446

have a great impact on the adsorption performance of the sample.

The repeated reuse of the adsorbent, that is, the stability of the adsorbent after multiple adsorption and desorption cycles, is a key criterion for judging the feasibility of the adsorbent in practical applications. To evaluate the regeneration performance of the prepared adsorbent, B-MC-F1 was selected for the CO_2 adsorption recycling test based on the above results. Figure 7d shows that after 10 adsorption and desorption cycles, although the adsorption capacity of CO_2 on the material decreases, it is still as high as 50 mg/g. We believe that the decrease in the adsorption performance of the material after multiple cycles is due to the disappearance or weakening of the pores in the material during the desorption process. This also shows that the adsorption of CO_2 by the material is mainly a physical adsorption process. The above results prove that B-MC-F1 has good adsorption and desorption cycling performance and reusability; therefore, B-MC-F1 can be used as an excellent solid adsorbent.

3. CONCLUSIONS

We have proposed a simple and feasible method to successfully prepare a series of B-doped mesoporous carbon materials with different boron-to-carbon molar ratios and template doses by hydrothermal synthesis (B-MC-*X* and B-MC-F*X*). All samples have interconnected pore structures and high boron contents. The prepared B-MC-F2 material has good electrocatalytic oxygen reduction to hydrogen peroxide performance in alkaline solution, which is closely related to its high specific surface area of 738 m^2/g, large total pore volume, and high oxygen content. In addition, the materials also show significant CO_2 capture capacity, and the optimal sample (B-MC-F1) has a CO_2 adsorption capacity of 121.34 mg/g at 303 K and atmospheric pressure; this adsorption capacity is far better than that of other B-doped mesoporous carbon materials. Based on the above structural features and their green production, boron-doped mesoporous carbon materials have broad application prospects for dealing with various environmental pollution problems.

4. EXPERIMENTAL SECTION

4.1. Material Synthesis. *4.1.1. Synthesis of B-MC-X.* In a topical procedure, 3.3 g of resorcinol and 0.4 mmol of F127 were dissolved in a mixture of ultrapure water (20 mL) and absolute ethanol (20 mL). Then, 120 μL of concentrated hydrochloric acid and a certain amount of boric acid were added into the solution and stirred for 60 min. Next, formaldehyde (2210 μL) was dripped into the solution and stirred vigorously for a period of time. The obtained mixed solution was then transferred into a reactor and placed in an oven at 100 °C for 72 h. The solution was cooled to room temperature, centrifugally washed thrice with water, and dried at 80 °C. Then, the obtained solid was carbonized at 600 °C for 3 h and was named B-MC-*X* (X = 1−4, wherein 1, 2, 3, and 4 represent B-to-C molar ratios of 0.025, 0.05, 0.075, and 1, respectively).

4.1.2. Synthesis of B-MC-FX. The effect of the amount of F127 on the material properties was studied. Based on the synthesis of B-MC-*X*, the amount of F127 was increased to 0.5 mmol to obtain B-MC-F1. When the amount of F127 was decreased to 0.2 mmol, B-MC-F2 was produced.

4.2. Physicochemical Characterization. High-resolution transmission electron microscopy (HRTEM) was carried out on a Tecnai G2F20 electron microscope (American FEI Company). X-ray diffraction (XRD) was conducted with a Rigaku UItima IV X-ray diffractometer using a Cu target and a Kα radiation source (λ = 0.1540 nm). At 77 K, using a pore physical adsorption instrument (ASAP 2020, Micromeritics), the N_2 adsorption and desorption isotherm of the material was obtained. Before testing, the material was degassed for 5 h at 100 °C and then the Brunauer−Emmett−Teller (BET) surface area was calculated based on the adsorption data (p/p_0 = 0.05−0.25). Raman spectra were measured by a Renishaw inVia microscope Raman spectrometer. The laser wavelength was 532 nm, and the scanning range was 100−4000 cm^{-1}. The IR spectrometer was produced by Nicolet, and the scanning range was 4000-400 cm^{-1}. The X-ray photoelectron spectroscopy (XPS) test of the material was carried out on a Kratos Axis Ultra DLD multifunction electronic spectrometer made in the U.K., with an Al Kα ($h\nu$ = 1486.6 eV) radiation source.

4.3. Electrochemical Testing. In regard to the ORR measurements, which were performed on an Autolab (Metrohm Autolab, Netherlands) electrochemical workstation, a typical three-electrode system was used with a catalyst-coated rotating disk electrode (RDE, 5 mm in diameter) as the working electrode and Hg/HgO and Pt wire used as the reference and counter electrodes, respectively. The preparation steps of the working electrode were as follows. All measured potentials were converted into reversible hydrogen electrode (RHE) scales by the following formula

$$E_{RHE} = E_{Hg/HgO} + 0.098 + 0.059 \times pH \quad (1)$$

The H_2O_2 generation yield and electron transfer number (n) were measured by the rotating ring-disk electrode (RRDE disk area: 0.2475 cm^{-2}). In the preparation of the working electrode, this can be calculated by the following equation

$$H_2O_2\ (\%) = 200 \times \frac{I_R/N}{I_R/N + I_D} \quad (2)$$

$$n = \frac{4I_D}{I_D + I_R/N} \quad (3)$$

Here, I_D and I_R represent the disk and ring currents, respectively, and the current collection efficiency (37%) of the Pt ring is represented by N. Briefly, 5 mg of the catalyst was added to a mixed solution consisting of 450 μL of ultrapure water, 500 μL of ethanol, and 50 μL of a 5 wt % Nafion solution. Then, this mixture was ultrasonically treated for 30 min to form a uniform slurry. Next, 16 μL of the prepared catalyst slurry was added dropwise on the upper part of the working electrode and dried at room temperature.

4.4. CO_2 Adsorption. Simulated flue gas was used to perform the CO_2 adsorption test on the material with a thermogravimetric analyzer (STA 449F5, NETZSCH). Before the adsorption test, a 5 mg sample was pretreated at 90 °C for 30 min and then a 50 mL/min CO_2 gas flow was maintained for 90 min of adsorption.

AUTHOR INFORMATION

Corresponding Author

Agula Bao − *Inner Mongolia Key Laboratory of Green Catalysis, College of Chemistry and Environmental Science, Inner Mongolia Normal University, Hohhot 010022, China;*

https://doi.org/10.1021/acsomega.1c00197
ACS Omega 2021, 6, 8438−8446

orcid.org/0000-0002-7859-9960; Phone: 0471-4393376; Email: agl@imnu.edu.cn

Authors

Jinhao Li − *Inner Mongolia Key Laboratory of Green Catalysis, College of Chemistry and Environmental Science, Inner Mongolia Normal University, Hohhot 010022, China*

Chao Shi − *Inner Mongolia Key Laboratory of Green Catalysis, College of Chemistry and Environmental Science, Inner Mongolia Normal University, Hohhot 010022, China*

Jingchun Jia − *Inner Mongolia Key Laboratory of Green Catalysis, College of Chemistry and Environmental Science, Inner Mongolia Normal University, Hohhot 010022, China*

Complete contact information is available at: https://pubs.acs.org/10.1021/acsomega.1c00197

Notes

The authors declare no competing financial interest.

■ ACKNOWLEDGMENTS

This work was supported by the Natural Science Foundation of Inner Mongolia of China (2016MS0212); the Collaborative Innovation Center for Water Environmental Security of Inner Mongolia Autonomous Region, China (XTCX003); the Science and Technology Program of Inner Mongolia Autonomous Region, China (2020PT0003); and the Applied Technology Research and Development Funds of Inner Mongolia Autonomous Region, China (2020GG0010).

■ REFERENCES

(1) Hu, L.; Cui, Y. Energy and environmental nanotechnology in conductive paper and textiles. *Energy Environ. Sci.* **2012**, *4*, 6423−6435.

(2) Thines, K. R.; Abdullah, E. C.; Mubarak, N. M.; Ruthiraan, M. Synthesis of magnetic biochar from agricultural waste biomass to enhancing route for waste water and polymer application: A review. *Renewable Sustainable Energy Rev.* **2017**, *67*, 257−276.

(3) Sivadas, D. L.; Vijayan, S.; Rajeev, R.; Ninan, K. N.; Prabhakaran, K. Nitrogen-enriched microporous carbon derived from sucrose and urea with superior CO_2 capture performance. *Carbon* **2016**, *109*, 7−18.

(4) Chen, Z.; Chen, S.; Siahrostami, S.; Chakthranont, P.; Hahn, C.; Nordlund, D. S.; Dimosthenis, J. K.; et al. Development of a reactor with carbon catalysts for modular-scale, low-cost electrochemical generation of H_2O_2. *React. Chem. Eng.* **2017**, *2*, 239−245.

(5) Siahrostami, S.; Verdaguer-Casadevall, A.; Karamad, M.; Deiana, D.; Malacrida, P.; Wickman, B.; Rossmeisl, J. Enabling direct H_2O_2 production through rational electrocatalyst design. *Nat. Mater.* **2013**, *12*, 1137−1143.

(6) Zabiegaj, D.; Caccia, M.; Casco, M. E.; Ravera, F.; Narciso, J. Synthesis of carbon monoliths with a tailored hierarchical pore structure for selective CO_2 capture. *J. CO_2 Util.* **2018**, *26*, 36−44.

(7) Kim, H. W.; Ross, M. B.; Kornienko, N.; Zhang, L.; Guo, J.; Yang, P.; McCloskey, B. D. Efficient hydrogen peroxide generation using reduced graphene oxide-based oxygen reduction electrocatalysts. *Nat. Catal.* **2018**, *1*, 282−290.

(8) Lu, Z.; Chen, G.; Siahrostami, S.; Chen, Z.; Liu, K.; Xie, J.; Cui, Y. High-efficiency oxygen reduction to hydrogen peroxide catalysed by oxidized carbon materials. *Nat. Catal.* **2018**, *1*, 156−162.

(9) Zhang, J.; Zhang, G.; Jin, S.; Zhou, Y.; Ji, Q.; Lan, H.; Liu, H.; Qu, J. Graphitic N in nitrogen-doped carbon promotes hydrogen peroxide synthesis from electrocatalytic oxygen reduction. *Carbon* **2020**, *163*, 154−161.

(10) Rehman, A.; Park, S. J. Environmental remediation by microporous carbon: An efficient contender for CO_2 and methylene blue adsorption. *J. CO_2 Util.* **2019**, *34*, 656−667.

(11) Zhang, W.; Bao, Y.; Bao, A. Preparation of nitrogen-doped hierarchical porous carbon materials by a template-free method and application to CO_2 capture. *J. Environ. Chem. Eng.* **2020**, *8*, 103732−103741.

(12) Chen, C.; Yu, Y.; He, C.; Wang, L.; Huang, H.; Albilali, R.; Cheng, J.; Hao, Z. Efficient capture of CO_2 over ordered micro-mesoporous hybrid carbon nanosphere. *Appl. Surf. Sci.* **2018**, *439*, 113−121.

(13) Zhao, C.; Jiao, Y.; Zhang, L.; Yang, Y. One-step synthesis of S, B co-doped carbon dots and their application for selective and sensitive fluorescence detection of diethylstilbestrol. *New J. Chem.* **2018**, *42*, 2857−2864.

(14) Rao, L.; Liu, S.; Wang, L.; Ma, C.; Wu, J.; An, L.; Hu, X. N-doped porous carbons from low-temperature and single-step sodium amide activation of carbonized water chestnut shell with excellent CO_2 capture performance. *Chem. Eng. J.* **2019**, *359*, 428−435.

(15) Lee, J. Y.; Lee, S. H.; Park, H. D. Enrichment of specific electro-active microorganisms and enhancement of methane production by adding granular activated carbon in anaerobic reactors. *Bioresour. Technol.* **2016**, *205*, 205−212.

(16) Yu, D.; Bai, J.; Wang, J.; Liang, H.; Li, C. Assembling formation of highly dispersed Pd nanoparticles supported 1D carbon fiber electrospun with excellent catalytic active and recyclable performance for Suzuki reaction. *Appl. Surf. Sci.* **2017**, *399*, 185−191.

(17) Ruiz, O. N.; Fernando, K. A. S.; Wang, B.; Brown, N. A.; Luo, P. G.; McNamara, N. D.; Bunker, C. E. Graphene Oxide: A nonspecific enhancer of cellular growth. *ACS Nano* **2011**, *5*, 8100−8107.

(18) Eftekhari, A.; Fan, Z. Ordered mesoporous carbon and its applications for electrochemical energy storage and conversion. *Mater. Chem. Front.* **2017**, *1*, 1001−1027.

(19) Lee, J.; Kim, J.; Hyeon, T. Recent progress in the synthesis of porous carbon materials. *Adv. Mater.* **2006**, *18*, 2073−2094.

(20) Szczęśniak, B.; Choma, J.; Jaroniec, M. Effect of graphene oxide on the adsorption properties of ordered mesoporous carbons toward H_2, C_6H_6, CH_4 and CO_2. *Microporous Mesoporous Mater* **2018**, *261*, 105−110.

(21) Bai, R.; Yang, M.; Hu, G.; Xu, L.; Hu, X.; Li, Z.; Fan, M. A new nanoporous nitrogen-doped highly-efficient carbonaceous CO_2 sorbent synthesized with inexpensive urea and petroleum coke. *Carbon* **2015**, *81*, 465−473.

(22) Guo, L.; Hu, X.; Hu, G.; Chen, J.; Fan, M. Tetraethylenepentamine modified protonated titanate nanotubes for CO_2 capture. *Fuel Process. Technol.* **2015**, *138*, 663−669.

(23) Li, C.; Yu, Z.; Liu, H.; Xiong, M. Synergetic contribution of Fe/Co and N/B dopants in mesoporous carbon nanosheets as remarkable electrocatalysts for Zinc-air batteries. *Chem. Eng. J.* **2019**, *371*, 433−442.

(24) Li, Z.; Guo, K.; Chen, X. Controllable synthesis of nitrogen-doped mesoporous carbons for supercapacitor applications. *RSC Adv.* **2017**, *7*, 30521−30532.

(25) Lei, Z.; Chen, H.; Yang, M.; Yang, D.; Li, H. Boron and oxygen-codoped porous carbon as efficient oxygen reduction catalysts. *Appl. Surf. Sci.* **2017**, *426*, 294−300.

(26) Zhao, H.; Hu, Z. P.; Zhu, Y. P.; Ge, L.; Yuan, Z. Y. P-doped mesoporous carbons for high-efficiency electrocatalytic oxygen reduction. *Chin. J. Catal.* **2019**, *40*, 1366−1374.

(27) Su, J.; Cao, X.; Wu, J.; Jin, C.; Tian, J. H.; Yang, R. One-pot synthesis of boron-doped ordered mesoporous carbons as efficient electrocatalysts for the oxygen reduction reaction. *RSC Adv.* **2016**, *6*, 24728−24737.

(28) Zhang, Q.; Huang, Y.; Xia, D.; Hu, L.; Li, P.; Yan, L.; Xie, Y. X. High-performance water desalination of heteroatom nitrogen- and sulfur-codoped open hollow tubular porous carbon electrodes via capacitive deionization. *Environ. Sci.: Nano* **2019**, *6*, 3359−3373.

(29) Zhu, L.; Gao, Q.; Tan, Y.; Tian, W.; Xu, J.; Yang, K.; Yang, C. Nitrogen and oxygen co-doped microporous carbons derived from the leaves of *Euonymus japonicus* as high performance supercapacitor electrode material. *Microporous Mesoporous Mater.* **2015**, *210*, 1−9.

(30) Ren, X.; Li, H.; Chen, J.; Wei, L.; Modak, A.; Yang, H.; Yang, Q. N-doped porous carbons with exceptionally high CO_2 selectivity for CO_2 capture. *Carbon* **2017**, *114*, 473−481.
(31) Wei, J.; Zhou, D.; Sun, Z.; Deng, Y.; Xia, Y.; Zhao, D. A controllable synthesis of rich nitrogen-doped ordered mesoporous carbon for CO_2 capture and supercapacitors. *Adv. Funct. Mater.* **2013**, *23*, 2322−2328.
(32) Park, J.; Nabae, Y.; Hayakawa, T.; Kakimoto, M. Highly selective two-electron oxygen reduction catalyzed by mesoporous nitrogen-doped carbon. *ACS Catal* **2014**, *4*, 3749−3754.
(33) Zhang, Y.; Qi, F.; Liu, Y. Fabrication of high B-doped ordered mesoporous carbon with 4-hydroxyphenylborate phenolic resin for supercapacitor electrode materials. *RSC Adv.* **2020**, *10*, 11210−11218.
(34) Zhao, R.; Li, Q.; Chen, Z.; Jose, V.; Huang, S. B, N-doped ultrathin carbon nanosheet superstructure for high-performance oxygen reduction reaction in rechargeable zinc-air batteries. *Carbon* **2020**, *164*, 398−406.
(35) Bo, X.; Guo, L. Ordered mesoporous boron-doped carbons as metal-free electrocatalysts for the oxygen reduction reaction in alkaline solution. *Phys. Chem. Chem. Phys.* **2013**, *15*, 2459−2465.
(36) Zhang, W.; Zhao, G.; Muschin, T.; Bao, A. Nitrogen-doped mesoporous carbon materials for oxidative dehydrogenation of propane. *Surf. Interface Anal.* **2021**, *53*, 100−107.
(37) Meng, Y.; Gu, D.; Zhang, F.; Shi, Y.; Yang, H.; Li, Z.; Yu, C.; Tu, B.; Zhao, D. Ordered mesoporous polymers and homologous carbon frameworks: amphiphilic surfactant templating and direct transformation. *Angew. Chem., Int. Ed.* **2015**, *117*, 7215−7221.
(38) Khai, T. V.; Na, H. G.; Kwak, D. S.; Kwon, Y. J.; Ham, H.; Shim, K. B.; Kim, H. W. Comparison study of structural and optical properties of boron-doped and undoped graphene oxide films. *Chem. Eng. J.* **2012**, *211−212*, 369−377.
(39) Song, J.; Zhang, Y.; Liu, Y. The influence of formaldehyde/phenol molar ratio on microstructure of B-OMCs. *RSC Adv.* **2015**, *5*, 20734−20740.
(40) Xin, W.; Song, Y.; Peng, J.; Liu, R.; Han, L. Synthesis of biomass-derived mesoporous carbon with super adsorption performance by an aqueous cooperative assemble route. *ACS Sustainable Chem. Eng.* **2017**, *5*, 2312−2319.
(41) Barman, M. K.; Jana, B.; Bhattacharyya, S.; Patra, A. Photophysical properties of doped carbon dots (N, P, and B) and their influence on electron/hole transfer in carbon dots-Nickel(II) phthalocyanine conjugates. *J. Phys. Chem. C* **2014**, *118*, 20034−20041.
(42) Pang, Y.; Wang, K.; Xie, H.; Sun, Y.; Titirici, M. M.; Chai, G. L. Mesoporous carbon hollow spheres as efficient electrocatalysts for oxygen reduction to hydrogen peroxide in neutral electrolytes. *ACS Catal* **2020**, *10*, 7434−7442.
(43) Lee, M. S.; Park, S. J. Silica-coated multi-walled carbon nanotubes impregnated with polyethyleneimine for carbon dioxide capture under the flue gas condition. *J. Solid State Chem.* **2015**, *226*, 17−23.
(44) Wu, D.; Yang, Y.; Liu, J.; Zheng, Y. Plasma-modified N/O-doped porous carbon for CO_2 capture: an experimental and theoretical study. *Energy Fuels* **2020**, *34*, 6077−6084.
(45) Jeon, D. H.; Min, B. G.; Oh, J. G.; Nah, C.; Park, S. J. Influence of nitrogen moieties on CO_2 capture of carbon aerogel. *Carbon Lett.* **2015**, *16*, 57−61.
(46) Li, L.; Wang, X. F.; Zhong, J. J.; Qian, X.; Song, S. L.; Zhang, Y. G.; Li, D. H. Nitrogen-enriched porous polyacrylonitrile-based carbon fibers for CO_2 capture. *Ind. Eng. Chem. Res.* **2018**, *57*, 11608−11616.
(47) Li, D.; Chen, Y.; Zheng, M.; Zhao, H.; Zhao, Y.; Sun, Z. Hierarchically structured porous nitrogen-doped carbon for highly selective CO_2 capture. *ACS Sustainable Chem. Eng.* **2015**, *4*, 298−304.

https://doi.org/10.1021/acsomega.1c00197
ACS Omega 2021, 6, 8438−8446